Plasma Sources Science and Technology

PURPOSE-LED PUBLISHING™

PAPER • OPEN ACCESS

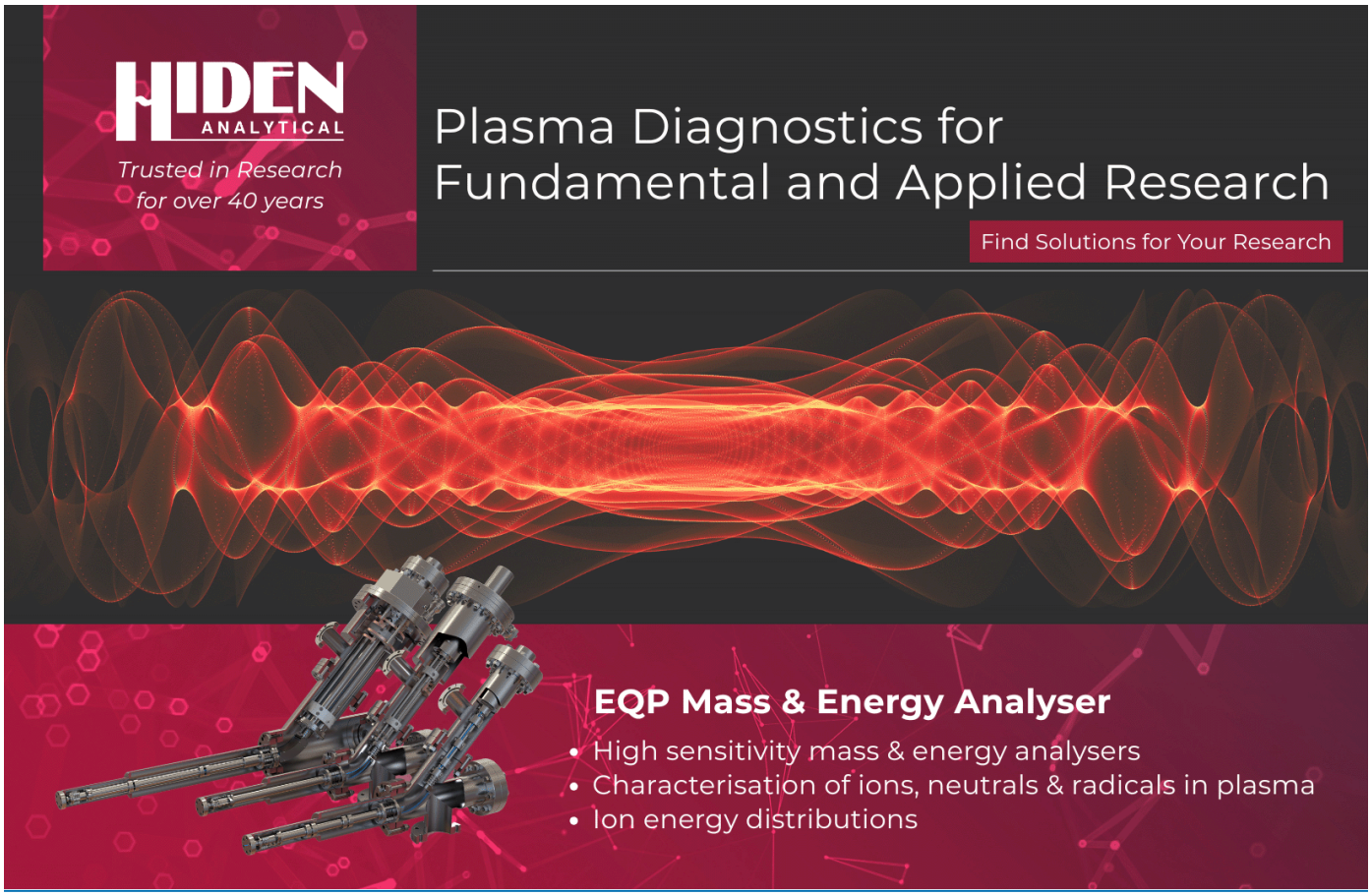
Mechanism of sidewall profile formation in plasma etching of Silicon trenches

To cite this article: V S Santosh K Kondeti *et al* 2026 *Plasma Sources Sci. Technol.* **35** 115001

View the article online for updates and enhancements.

You may also like

- Effects of surface microstructure on atmospheric-air repetitive single-filament DBD
Liyang Zhang, Jiacun Wu, Dong Yang et al.
- Mechanism study on enhancing the helicon plasma density in the target region of linear plasma device MPS-LD
Jintao Wu, Changjiang Sun, Chaofeng Sang et al.
- Bayesian analysis and uncertainty quantification of model parameters in radio blackout prediction
Yunlong Xue, Yuhang Hou, Yongliang Feng et al.



This content was downloaded from IP address 136.226.20.91 on 18/11/2026 at 21:50

Plasma Sources Science and Technology

Check for updates

OPEN ACCESS

RECEIVED
11 May 2026

REVISED
30 August 2026

ACCEPTED FOR PUBLICATION
14 October 2026

PUBLISHED
3 November 2026

Original content from this work may be used under the terms of the Creative Commons Attribution 4.0 licence.

Any further distribution of this work must maintain attribution to the author(s) and the title of the work, journal citation and DOI.

PAPER

Mechanism of sidewall profile formation in plasma etching of Silicon trenches

V S Santosh K Kondeti[1,*], **Leonid Dorf**[2], **Zihao Ding**[2], **Sonam D Sherpa**[2], **Takumi Yanagawa**[2], **Leonid Belau**[2] and **Yevgeny Raitses**[1]

[1] Princeton Plasma Physics Laboratory, Princeton, NJ, United States of America
[2] Applied Materials, Santa Clara, CA, United States of America
[*] Author to whom any correspondence should be addressed.

E-mail: vkondeti@pppl.gov

Keywords: laser-induced fluorescence, plasma etching, pulsed inductively coupled plasma, plasma chemistry, SiCl, $SiCl_2$, sidewall profile control

Abstract

In isolated features, such as silicon trenches, of a patterned semiconductor substrate a sidewall taper during chlorine-based plasma etching originates from the deposition of chemical by-products on the sidewall, which progressively shifts the boundary of the etchable horizontal surface outwards. This deposition can be mitigated by controlling the gas-phase radical densities using power pulsing schemes. Our time-resolved laser-induced fluorescence measurements of $SiCl_2$ radicals and the high-sticking-coefficient SiCl radicals reveal that their density is governed by the absolute on- and off-times. The observed density behavior suggests that SiCl radicals are: (a) produced through a combination of higher silicon chlorides ($SiCl_{2-4}$) dissociation by electron-impact and metastable-assisted processes, and direct surface-generated pathways, with dissociation of species such as $SiCl_2$ making a major contribution under the present experimental conditions, and (b) lost primarily through rapid gas-phase reactions and wall losses, rather than through evacuation from the chamber. The presence of argon in the plasma enhances the density and persistence of SiCl radicals while simultaneously reducing the gas-phase density of $SiCl_2$, suggesting that argon substantially modifies the plasma kinetics responsible for the dissociation of higher silicon chlorides ($SiCl_{2-4}$), potentially through an increase in electron density and argon metastable assisted reactions. We further show that for sufficiently long on- and short off-times, SiCl radicals are produced from the start of the on-phase with their density reaching saturation and subsequently decaying in the afterglow, yielding a tapered isolated sidewall profile. Conversely, for sufficiently long off-times allowing the loss of a significant portion of $SiCl_2$ radicals, the SiCl density growth during the on-phase experiences a marked delay, so selecting sufficiently short on-time allows reducing SiCl gas-phase density by an order of magnitude and achieving a desired nearly vertical sidewall profile. The features profiles in this work were imaged using transmission electron microscopy.

1. Introduction

The fabrication of high fidelity etch features in silicon is a cornerstone of advanced semiconductor manufacturing, microelectromechanical systems, and nanoscale device engineering [1]. As device geometries shrink, achieving precise, anisotropic etch profiles becomes increasingly critical [2, 3]. Plasma-based etching techniques, particularly those employing chlorine-containing chemistries such as Ar/Cl_2 mixtures, have emerged as the preferred approach due to their superior selectivity, pattern fidelity, and reduced chemical waste compared to wet etching methods [3].

In reactive ion etching of Si in Cl_2/Ar gas mixture, chlorine radicals generated in the plasma adsorb onto the silicon surface to form volatile silicon-chloride species ($SiCl_x$, $x = 1-4$) [4, 5]. Chemisorbed chlorine breaks Si–Si bonds and forms volatile $SiCl_x$ species at the surface. These species have significantly lower desorption energies than the Si–Si bonds in crystalline silicon, enabling efficient material

© 2026 The Author(s). Published by IOP Publishing Ltd

removal [6–8]. These species are subsequently desorbed or sputtered from the wafer surface under the influence of a bias voltage, which accelerates ions toward the substrate [9]. Among these, SiCl exhibits a larger desorption energy (4.52–5.74 eV), compared to $SiCl_2$ (1.65–3.2 eV) [6–8, 10–14]. SiCl has been reported to have a near unity sticking coefficient [4, 15] making it particularly prone to re-deposition on the wafer surface. Such deposition can be controlled by using various plasma power pulsing schemes, where the duty cycle (DC) and on-off times are adjusted to tune the radical densities during the pulse cycle. During etching of patterned semiconductor substrates, an undesired taper of the etched sidewall, especially in isolated trenches, arises not only from ineffective directional ion bombardment but also from the progressive deposition of high sticking coefficient species. Such high sticking coefficient species can be produced by the by-products of etching, sputtering of the mask and plasma-wall interaction processes that generate additional reactive species. These species deposit on the regions adjacent to an isolated mask to form a passivation layer, which behaves differently to ion bombardment compared to the material being etched such as silicon. As this layer accumulates over time, it inhibits removal of the underlying silicon, effectively shifting the boundary of the etchable horizontal surface outward in time over multiple etch cycles. This results in the formation of a tapered isolated sidewall over time, set by a balance between the time dependent radical production-loss processes and ion-driven removal.

In this work, we investigate the generation and decay of SiCl and $SiCl_2$ radicals produced during the etching of a bare silicon wafer in a pulsed inductively coupled reactor equipped with a pulsed direct current bias [16–19]. Using in-situ laser-induced fluorescence (LIF) diagnostics, we quantified the time-resolved behavior of SiCl and $SiCl_2$ radicals under various pulsing conditions. While SiCl radicals can originate from dissociation pathways of $SiCl_{2-4}$, $SiCl_3$ and $SiCl_4$ are not directly accessible with LIF and we focus on $SiCl_2$-derived pathways. These measurements are correlated with ex-situ transmission electron microscopy (TEM) analysis of etched silicon features. We focus on one important sidewall taper formation pathway involving silicon chloride radicals, while recognizing that additional pathways, including those involving oxygen-containing species and oxide formation, may also contribute to sidewall deposition. Our findings demonstrate that reducing the gas-phase SiCl density by an order of magnitude significantly reduces the isolated line sidewall taper.

2. Methods

2.1. Plasma apparatus

The reactor used in this work consisted of a cylindrical aluminum liner coated with yttrium oxide, with its interior dimensions measuring 62 cm in diameter and 15 cm in height, housed within a vacuum vessel. The chamber was evacuated using a turbo-molecular pump supported by a roughing pump, achieving base pressures on the order of 1 μTorr. The operating pressure was maintained at 15 mTorr using mass flow controllers and a control valve. The chamber walls and the lid were maintained at a temperature of 65° C and 80° C respectively. A bare silicon wafer with a diameter of 300 mm was mounted on an electrostatic chuck positioned on top of the bottom electrode. The used wafer was cut along the Si(100) crystallographic plane and chucked by a voltage of 3000 V and helium backside flow. Although the wafer temperature was not actively regulated, a coolant maintained at 20° C circulated through a metallic support plate.

An inductively coupled plasma (ICP) reactor with a pulsed bias (PB) voltage manufactured by Applied Materials was used to etch the silicon wafer [16]. The chamber of the reactor was fitted with multiple sapphire viewports to facilitate optical diagnostics. The antenna for the ICP source was on top of a ceramic lid. A 13.7 MHz radio-frequency (RF) power was applied to the antenna of the ICP source. An RF power of 1 kW was applied to the ICP antenna. The RF power was operated in a pulsed mode, characterized by a modulation frequency referred to as the macro-frequency [16–19]. The RF power was modulated using a defined DC, the plasma turning on during a specific portion of each macro-frequency cycle. In this work, macro-frequencies of 100 Hz and 20 Hz were used. For example, a macro-frequency of 100 Hz and a DC of 70% corresponds to the RF power being on for a time period (T_{on}) of 7 ms within the 10 ms period. Unless otherwise specified, an 800 V PB voltage amplitude at a frequency of 400 kHz was synchronously applied to the substrate in coordination with the RF power modulation. The DC of the PB voltage was 50%. So, the PB voltage was applied for 1.25 μs within each 2.5 μs period. The PB voltage accelerates the RF plasma generated ions towards the wafer surface. A plasma afterglow exists after all power is turned off. The used off-times in this work were significantly larger than the plasma decay time in the reactor. Unless otherwise specified, a gas mixture comprising 50 sccm each of argon and chlorine (50% Ar + 50% Cl_2) was introduced into the reactor using mass flow controllers. After placing the wafer inside the chamber, a breakthrough step using a gas mixture of CF_4 +

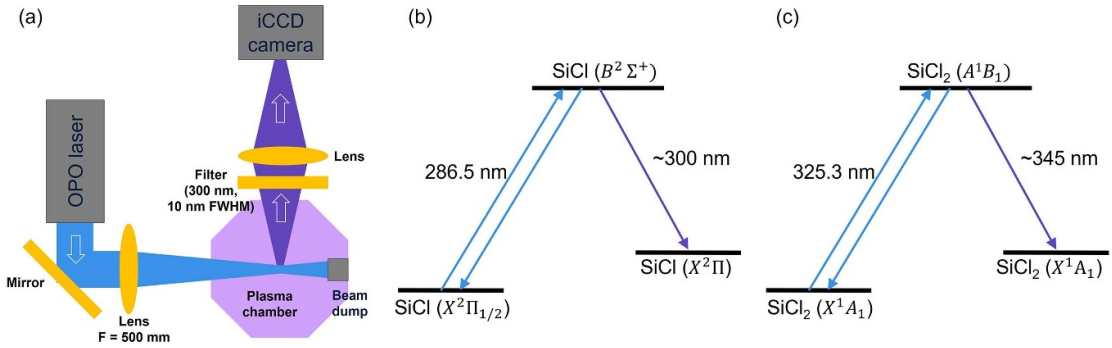


Figure 1. (a) Schematic of the laser induced fluorescence setup. LIF transition scheme of (b) SiCl radicals and (c) $SiCl_2$ radicals.

Ar plasma was operated in a CW mode with an RF power of 200 W and a PB voltage of 150 V was run for 10 s to remove native oxide from the wafer prior to running the Ar + Cl_2 plasma. After each run of the Cl_2 containing plasma, the wafer was retrieved from the reactor and the reactor was cleaned using an RF NF_3 + O_2 plasma without bias voltage.

2.2. Laser induced fluorescence

LIF diagnostic was used to measure the relative densities of SiCl and $SiCl_2$ radicals [20–29]. A nanosecond pulsed optical parametric oscillator (OPO) laser (Ekspla NT-230, 100 Hz) was used to excite these radicals. Figures 1(a)–(c) show the experimental setup, the used LIF transition schemes for SiCl and $SiCl_2$ respectively. The fluorescence was imaged on to a fiber optics cable (Thorlabs M112L02, 200 μm) by a UV fused silica lens with a focal length of 200 mm and detected by the iCCD camera (Andor, DH334T) coupled to a spectrometer (Princeton Instruments, HRS750) to confirm the LIF spectrum. After confirming the SiCl and $SiCl_2$ LIF spectrum, the LIF signal was imaged through a bandpass filter directly on to the iCCD camera by an objective lens (Nikon UV-105). All LIF data presented in this work were acquired using the bandpass filter configuration.

SiCl radicals were detected by tuning the laser to 286.5 nm to excite SiCl radicals from the SiCl($X^2\Pi_{1/2}$) level to the SiCl($B^2\Sigma^+$) level [20–24]. The center of the excitation transition wavelength was obtained by scanning the laser wavelength to find the maximum fluorescence intensity. Fluorescence around a wavelength of 300 nm was detected during the de-excitation from the SiCl ($B^2\Sigma^+$) level to the SiCl ($X^2\Pi$) level by the iCCD camera. The maximum laser energy at 286.5 nm was 450 μJ/pulse. The laser energy was reduced to 1.4 μJ/pulse to be in the linear LIF regime by using a neutral density filter, ensuring that the fluorescence signal is directly proportional to the radical density and is not affected by saturation or nonlinear excitation effects. An optical bandpass filter (Edmund optics #35–884, centered at 300 nm with a full width at half maximum (FWHM) of 10 nm) was used to collect the SiCl LIF intensity. The camera gate was set to 90 ns to collect all the fluorescence signal for a period of 90 ns from the start of the laser beam excitation.

$SiCl_2$ radicals were detected using LIF by tuning the OPO laser to 325.3 nm to excite $SiCl_2$ from the ground electronic state $SiCl_2(X^1A_1)$ to a vibrationally excited level of the $SiCl_2(A^1B_1)$ electronic state [26–29]. Fluorescence was observed in the 340–360 nm wavelength range, arising from the decay of the $SiCl_2(A^1B_1)$ state to the $SiCl_2(X^1A_1)$ state. The maximum laser energy at 325.3 nm was about 540 μJ/pulse. Similar to the case of SiCl LIF, the laser energy for $SiCl_2$ LIF was reduced to 1.7 μJ/pulse to be in the linear LIF regime by using a neutral density filter. A bandpass filter (Thorlabs, FBH343-10, centered at 343 nm with an FWHM of 10 nm) was used to collect the LIF signal. The camera gate was set to 205 ns to capture the fluorescence signal for a period of 205 ns after the excitation by the laser beam.

The laser beam was radially focused into the center of the chamber using a 500 mm focal length fused silica planoconvex lens at a height of 2 cm above the wafer surface. The camera captured both the LIF signal and background plasma emission. The LIF signal intensity at different phases of the pulsed plasma operation was calculated by subtracting the background signal measured when the laser wavelength was de-tuned entirely from the used LIF transition wavelength from the signal measured when the laser wavelength was tuned to the LIF transition wavelength. The LIF measurements represent an average over a length of 1 cm along the laser propagation axis, centered 2 cm above the wafer surface. The reported data is an average of at least five measurements. A delay generator (Berkeley Nucleonics, BNC 575) was used to synchronize the laser beam and the iCCD camera with the macro pulse of the plasma reactor. The LIF signal intensity was accumulated over a camera integration time of 0.75–6 s.

To compare different measurement conditions, the LIF intensity was normalized to camera integration time. The LIF measurements were performed after the Ar + Cl_2 plasma was run for at least 3 minutes to enable reproducible measurements. The same Si(100) wafer was used for several LIF measurement conditions. The used Si wafer was replaced with a new Si wafer when the thickness of the wafer reduced below 0.5 mm.

2.3. TEM of etched features

To investigate the impact of pulsing parameters on the sidewall taper of the isolated features, Si(100) lines patterned with a 60 nm thick Si_3N_4 hard mask were etched by placing a 2 cm x 2 cm coupon on a Si_3N_4 wafer with a diameter of 300 mm. The coupon consisted of isolated and dense patterns. The etch recipe began with a breakthrough step containing CF_4 plasma to remove the native oxide on the wafer followed by exposure to an Ar + Cl_2 plasma to etch the Si(100) lines. The etched structures were imaged using cross-sectional TEM. TEM imaging was performed using Thermo Scientific Talos F200E operating at 200 kV, enabling high-resolution imaging of the etch profiles. The etch sidewall taper of the isolated etch features was compared for four pulsed plasma operation conditions (table 2). All four conditions consisted of synchronous pulsing in which both the RF power and PB were simultaneously applied. Cases (a) and (b) have the same T_{on}, but different T_{off}. Cases (c) and (d) have different T_{on}, while they have the same T_{off}.

3. Results and discussion

3.1. Effect of wall deposition

Figure 2 compares the effect of the wall condition and ion bombardment on SiCl and $SiCl_2$ production in a continuous-wave plasma by comparing three different plasma and wall conditions. In case I and case III, only RF power was applied, while in case II both RF power and PB were simultaneously applied. A new bare silicon wafer was placed inside the chamber and the experiment was performed sequentially according to the following steps: a breakthrough step to remove native oxide from the wafer surface, followed by case I, case II and case III (figure 2). Case I was run for 35 min, during which the silicon wafer was etched by the RF plasma. This was followed by case II for 1 hour, where ions from the RF plasma were bombarded onto the wafer by the application of the PB. The subsequent case III step was run for 35 min with only the RF plasma and no PB. Because of this sequence, case I started with nearly clean chamber walls containing little $SiCl_x$ ($x = 1-4$) deposition. In contrast, the walls contained increasing amounts of deposited $SiCl_x$ ($x = 1-4$) at the beginning of case II and case III. The application of PB in case II enhances the etch rate of the wafer and increases the deposition of $SiCl_x$ species on the chamber walls. In case III, the removal of the PB results in lower deposition rates than in case II and the chamber walls progressively become cleaner with time.

Both $SiCl_2$ and SiCl are detected in case I, although their densities remain close to the detection limit of the LIF diagnostics and increase only gradually during this 35 min step. The RF plasma dissociates Cl_2 gas molecules to form Cl radicals, which adsorb onto the wafer surface. Although no PB is applied in this step, measurable etching still occurs due to the RF plasma, resulting in the removal of $SiCl_x$ ($x = 1-4$) species from the wafer surface. Starting with clean chamber walls in case I, the detected SiCl and $SiCl_2$ densities remain very low. When the PB is turned on in case II, the densities of both SiCl and $SiCl_2$ increase rapidly before reaching saturated values. In this step, the PB accelerates ions toward the wafer surface and enhances the removal of $SiCl_x$ ($x = 1-4$) species from the wafer. The SiCl density saturates after approximately 10 min of operation, while $SiCl_2$ reaches saturation after about 25 min. The gradual increase in both SiCl and $SiCl_2$ over tens of minutes is significantly longer than the characteristic production and decay times of these radicals and therefore reflects progressive conditioning of the chamber walls and the establishment of a balance between deposition and removal of silicon chlorides. The measured SiCl and $SiCl_2$ densities in case II are significantly higher than those measured in case I. The presence of the PB increases the etch rate of silicon and generates substantially higher gas-phase densities of SiCl and $SiCl_2$ radicals. The detected SiCl and $SiCl_2$ radicals in this step originate from both the wafer surface and the chamber walls. The case II step was run for a time period of one hour, however the measurements of SiCl and $SiCl_2$ were only performed for 35 minutes into case II. By the end of the 1 hour duration of case II, the chamber walls contain substantial $SiCl_x$ ($x = 1-4$) deposition.

In case III, the PB is turned off and only RF plasma is present. The deactivation of the PB leads to a substantial reduction in the SiCl and $SiCl_2$ densities, reflecting the loss of a major wafer-originated production pathway for these species. To investigate the source of SiCl and $SiCl_2$ radicals under these conditions, measurements were performed both with and without a wafer present inside the chamber.

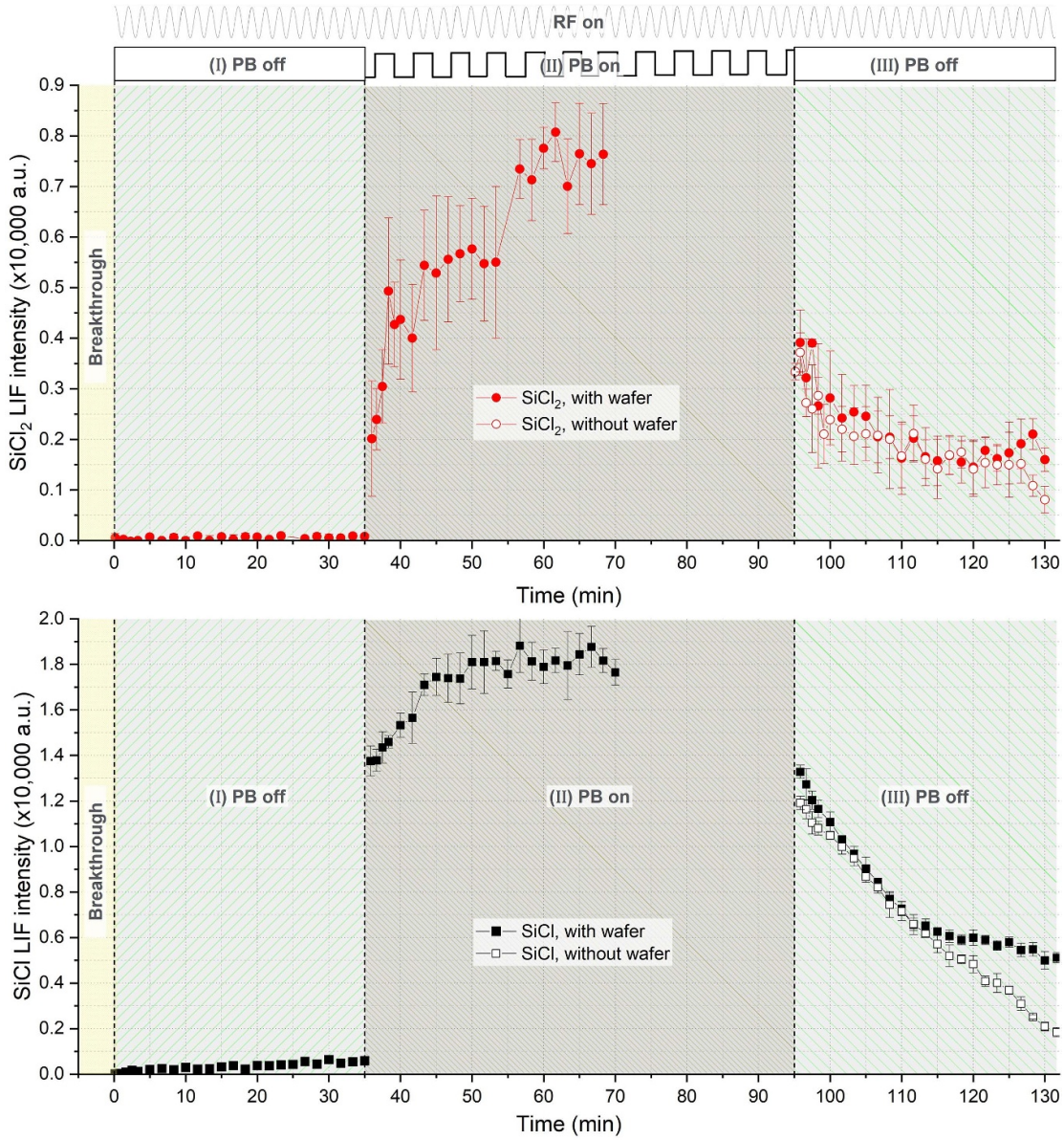


Figure 2. The effect of walls and pulsed bias voltage in a CW RF plasma at a distance of 2 cm above the center of the wafer. The recipe starts with a breakthrough step to remove native oxide from the wafer, followed by CW plasmas with: (I) No pulsed bias from 0–35 min (starts with clean walls), (II) With pulsed bias from 35–95 min (starts with dirty $SiCl_x$ ($x = 1 - 4$) deposited walls), and (III) No pulsed bias from 95–135 min (starts with a dirty $SiCl_x$ ($x = 1 - 4$) deposited walls).

Although these measurements were performed at different times, the same step I and step II recipe conditions were used prior to case III to ensure equivalent wall conditioning. Both SiCl and $SiCl_2$ densities decrease with the progression of time in case III. The $SiCl_2$ density decreases rapidly during the first 10–15 min before approaching a quasi-steady-state value. With the progression of case III, the amount of silicon chloride present on the chamber walls is expected to decrease as the deposited material is gradually removed, chemically transformed, pumped away, or returned to the plasma. The $SiCl_2$ density measured with and without a wafer present in the chamber are nearly identical during the initial portion of case III, indicating that chamber-wall-derived species dominate the observed $SiCl_2$ density immediately after PB removal. Approximately 30 min into case III, the two curves begin to diverge, with the no-wafer condition producing a lower $SiCl_2$ density. This behavior indicates that while the chamber walls remain a significant source of $SiCl_2$, continued production from the wafer contributes measurably once the chamber-wall reservoir is progressively depleted. The time evolution of the SiCl radicals in case III is similar for both the wafer and no-wafer conditions during the initial part of the step. However, the SiCl density measured without a wafer decreases more rapidly than that measured with a wafer present. The

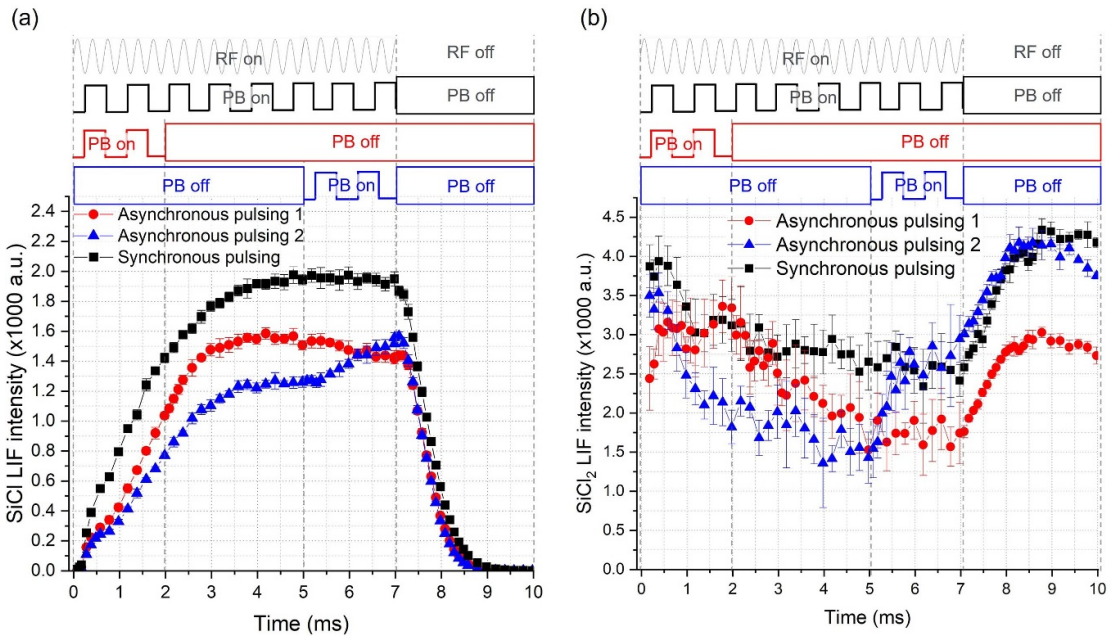


Figure 3. The time-resolved evolution for synchronous and asynchronous conditions described in table 1 of (a) SiCl LIF intensity and (b) $SiCl_2$ LIF intensity. RF power is applied from 0–7 ms for synchronous and asynchronous pulsing cases. PB is on from 0–2 ms for asynchronous pulsing 1, from 5–7 ms for asynchronous pulsing 2, and from 0–7 ms for synchronous pulsing conditions. All power is off from 7–10 ms.

Table 1. The synchronous and asynchronous pulsing characteristics for conditions used in figure 3. The macro-frequency and duty cycle were 100 Hz and 70% respectively. The RF is on for a time of 7 ms within the 10 ms period.

Case	PB on-time (ms)	PB location
Asynchronous pulsing 1	2	Start of RF
Asynchronous pulsing 2	2	End of RF
Synchronous pulsing	7	Throughout RF

divergence becomes increasingly pronounced with time, indicating that both the chamber walls and the wafer contribute to the observed SiCl density. As the wall reservoir progressively depletes, the contribution from wafer-generated precursor species becomes increasingly important.

These measurements demonstrate that the chamber walls act as a significant reservoir of silicon chloride species. The increase of SiCl and $SiCl_2$ during case II and their persistence after removal of the PB in case III indicate that previously deposited silicon chlorides continue to contribute to the measured radical densities. The comparison between the wafer and no-wafer conditions further shows that both the wafer and chamber walls contribute to the observed SiCl and $SiCl_2$ populations, with the wall contribution dominating immediately after PB removal and the wafer contribution becomes important as the wall reservoir begins to get depleted.

3.2. Effect of synchronous and asynchronous pulsing

We now consider how the time modulation of RF power and PB influences the production and decay of SiCl and $SiCl_2$ radicals in pulsed discharges. Consider a macro-frequency of 100 Hz with a DC of 70%, so the RF power is on for 7 ms and all power is off for 3 ms. Figures 3(a) and (b) shows the SiCl and $SiCl_2$ densities respectively for three different pulsing conditions described in table 1, where the PB is applied at different locations within the RF on-time. In the asynchronous pulsing configurations, the PB voltage was applied for a duration of 2 ms, either at the beginning of the RF on-phase (0–2 ms, asynchronous pulsing 1) or at the end of the RF on-phase (5–7 ms, asynchronous pulsing 2). In the synchronous pulsing condition, the PB was applied continuously throughout the entire RF on-phase (0–7 ms).

Figure 3(a) shows that irrespective of whether you apply the PB voltage for 2 ms at the start of the RF, 2 ms at the end of the RF or for the entire 7 ms duration of the RF, SiCl is produced from the start

of the RF for all cases. This suggests that the measured SiCl density is not determined solely by the timing of PB application and is strongly influenced by RF-plasma driven processes. The measured SiCl density is strongly determined by gas-phase dissociation of $SiCl_x$ ($x = 2-4$), with $SiCl_2$ likely acting as a major precursor [15]. The early rise of SiCl observed under synchronous bias may include contributions from ion-assisted surface release, in addition to prompt gas-phase processes [4]. The saturated SiCl density for the synchronous pulsing case is larger than the asynchronous pulsing cases suggesting that the precursor species for the formation of SiCl, such as $SiCl_2$ is larger in density for the synchronous pulsing case where PB voltage is applied for a longer time period. The primary etch byproduct is produced when PB voltage is applied. The SiCl density for the two asynchronous pulsing cases reach similar densities by the end of the RF power on-phase, irrespective of where the PB voltage is applied with respect to the RF power. Figure 3(a) indicates that direct ion-assisted release from the wafer cannot by itself explain the observed temporal evolution of SiCl. The similar time-resolved evolution of SiCl observed for all three pulsing conditions suggests that the measured SiCl density is not determined solely by the instantaneous ion bombardment of the wafer. While PB controls the release of silicon chloride precursors from the surface, the subsequent production of SiCl appears to be governed predominantly by RF-plasma-driven processes. The fact that comparable SiCl densities are obtained irrespective of whether the PB is applied at the beginning, the end, or throughout the RF-on phase indicates that gas-phase formation pathways involving higher silicon chlorides make a major contribution to the measured SiCl density for our experimental conditions. However, we note that both molecular dynamics simulations and time-resolved optical emission spectroscopy measurements have shown that SiCl can also be produced directly as an etch product from chlorinated silicon surfaces during ion bombardment [30, 31]. The asynchronous pulsing 2 case shows an increase in SiCl density after 5 ms when PB is applied, coinciding with the increase in $SiCl_2$ density shown in figure 3(b). Figure 3(b) shows the $SiCl_2$ density for the synchronous and asynchronous pulsing cases. Let us first consider the RF on phase. For the synchronous pulsing case, the $SiCl_2$ density stays nearly constant for the duration of the synchronous RF + PB phase. For asynchronous pulsing 1 case, the $SiCl_2$ density increases for the first 2 ms when the PB is applied and drops when the PB is turned off before settling at a steady state value towards the end of the RF on phase. For asynchronous pulsing 2 case, the $SiCl_2$ density drops at the start of the RF on phase and reaches a steady state region. When the PB is applied at 5 ms, we observe an increase in the $SiCl_2$ density due to ion bombardment on the wafer which releases $SiCl_2$ into the gas phase. For all the three pulsing schemes, the $SiCl_2$ density increases after all power is turned off (7–10 ms) during which there is a drop in the SiCl density. This is likely due to the gas phase recombination of SiCl radicals with Cl_2 molecules producing additional $SiCl_2$ and Cl radicals [15]. In addition, spatial gas-temperature gradients between the edge of the chamber and the center of the chamber may contribute to the transient increase in $SiCl_2$ density during the off-phase, although gas temperatures were not measured in the present study. Under the present experimental conditions, the transient behavior of SiCl production is strongly influenced by the evolution of $SiCl_2$, while other silicon chlorides ($SiCl_3$ and $SiCl_4$) contribute to the overall precursor pool.

3.3. The effect of macro-frequency and DC

Figures 4(a) and (b) compares the normalized SiCl LIF intensity for the four conditions described in table 2. The LIF intensity for each condition was normalized to its LIF intensity at the end of the on-phase. Figure 4(a) shows the growth of SiCl for these four conditions. The RF power and the PB voltage were applied synchronously from $T = 0$ ms. In high DC conditions (cases (a) and (c)), SiCl radicals were generated immediately upon plasma ignition ($T = 0$ ms), whereas low DC conditions (cases (b) and (d)) exhibited a delayed onset of SiCl production. This delay in onset is greater for case (b) ($T_{off} = 43$ ms) compared to case (d) ($T_{off} = 8$ ms). SiCl is produced by the gas-phase electron impact dissociation of higher silicon chlorides such as $SiCl_2$, $SiCl_3$ and $SiCl_4$ [4, 15]. Figure 5(b) shows that $SiCl_2$ is lost completely within about 20 ms during the 43 ms off-time for case (b), while it decreases by about an order of magnitude for case (d) during the 8 ms off-time. The buildup of precursor species ($SiCl_{2-4}$), with $SiCl_2$ likely acting as a dominant source of SiCl radicals under our present conditions, is faster for case (d) compared to case (b) when the next on-phase starts (figure 5(b)), as case (b) starts with no residual $SiCl_2$ density by the end of the off-phase. This is consistent with the work of Cunge *et al* [32], who showed that in a similar ICP plasma chamber with Ar + Cl_2 + $SiCl_4$ gas composition at a pressure of 10 mTorr, the $SiCl_2$ radicals were completely removed from the chamber in about 20 ms after turning off the power. A long T_{off} of 43 ms for case (b) results in complete removal of $SiCl_2$ from the chamber during the off-time phase through diffusion to the chamber walls and evacuation by the vacuum pump. The delay in SiCl production with respect to the on-phase is a result of time taken to build up the density of higher silicon chlorides such as $SiCl_2$, $SiCl_3$ and $SiCl_4$ after PB voltage is applied and

Table 2. The macro-frequency properties with the on-time and the off-times for the four different synchronous pulsing conditions.

Case	Macro-freq.(Hz)	Duty cycle %	Period (ms)	On-time (T_{on}) (ms)	Off-time(T_{off}) (ms)
(a)	100	70	10	7	3
(b)	20	14	50	7	43
(c)	20	84	50	42	8
(d)	100	20	10	2	8

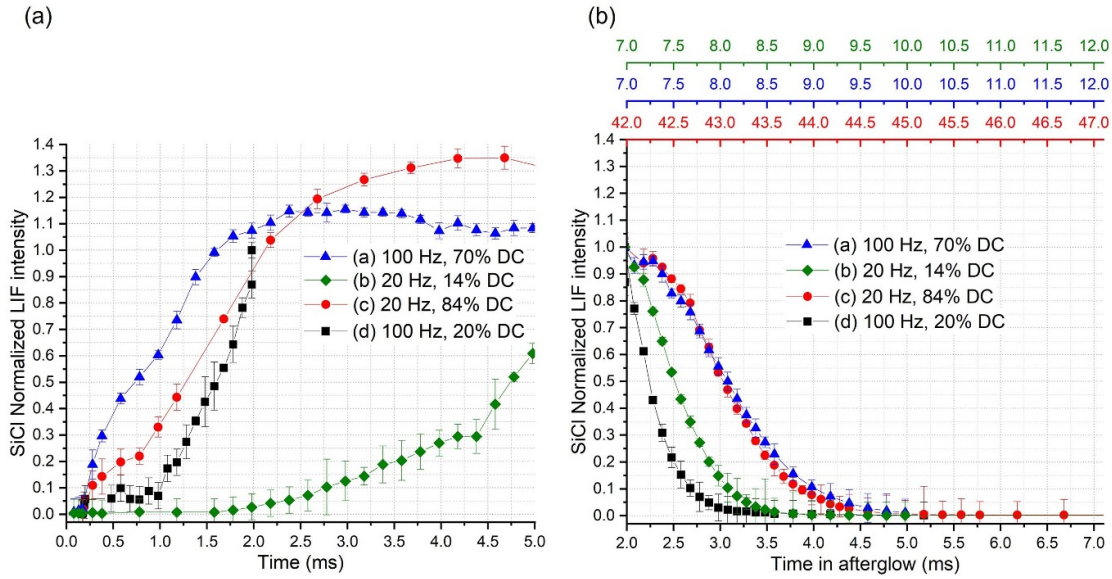


Figure 4. The time-resolved evolution of the normalized SiCl LIF intensity for four conditions described in table 2. (a) Growth during the start of the on-phase (b) Decay after all power is off.

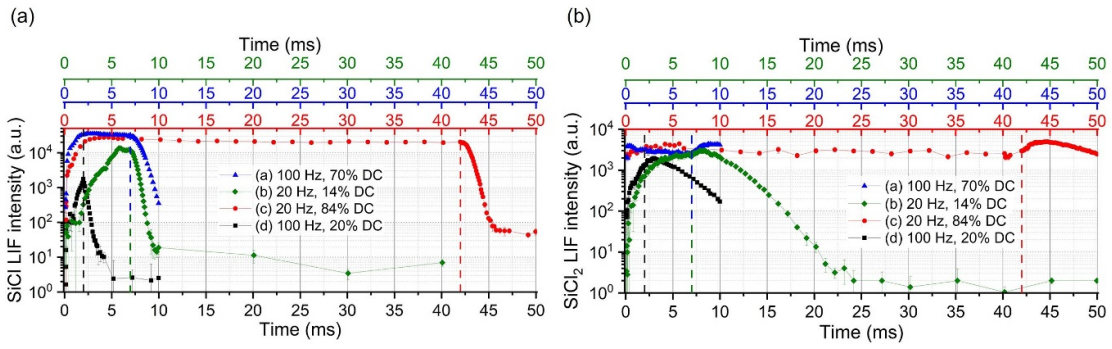


Figure 5. The time-resolved evolution for the four conditions described in table 2 of (a) SiCl LIF intensity and (b) $SiCl_2$ LIF intensity. The color coded vertical dotted lines show the end of the synchronous power on-phase for each condition.

the subsequent production of SiCl from them. Case (d), with $T_{off} = 8$ ms, also exhibited delayed SiCl radical production with respect to the on-phase. While $SiCl_2$ is not completely removed from the chamber during this 8 ms off-time, a smaller density of $SiCl_2$ is generated during the 2 ms on-time results, which decays by nearly an order of magnitude by the end of the 8 ms off-phase. The observed growth of SiCl at the start of the on-phase reflects the balance between its production and loss processes. At the start of the on-phase, the density of silicon chloride precursors is low and the SiCl production rate is insufficient to balance losses through gas-phase reactions and surface interactions. As the precursor density increases, the SiCl production rate rises until a quasi-steady-state density is reached when production and loss become approximately balanced.

Figure 4(b) shows the decay of SiCl radicals after all power is turned off. SiCl radicals decay similarly for the large DC cases of conditions (a) and (c). However, despite having the same on-time of 7 ms (condition (a) and (b)), SiCl radicals decay faster for condition (b) where the off-time is larger.

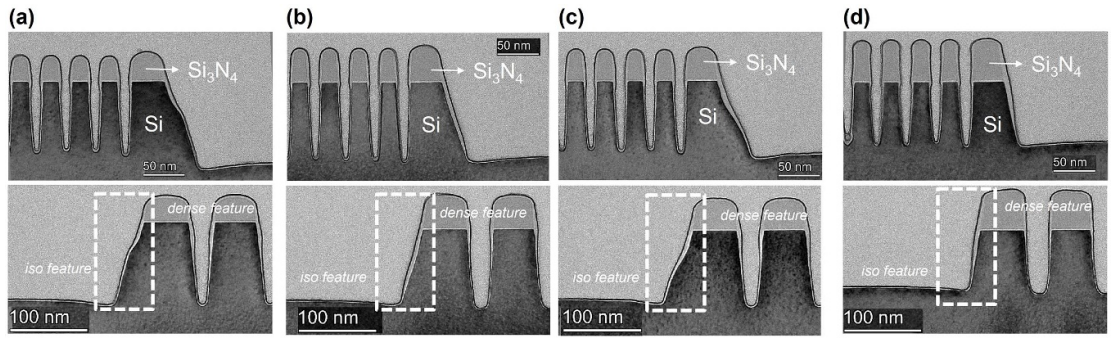


Figure 6. TEM images for the four conditions described in table 2. The etch time was adjusted to achieve similar etch depths. The pitch/space critical dimension (CD) of the top row images and bottom row images are 36 nm/18 nm and 90 nm/45 nm respectively. The macro-frequency and duty cycle are: (a) 100 Hz & 70% DC, (b) 20 Hz & 14% DC, (c) 20 Hz & 84% DC and (d) 100 Hz & 20% DC. The blanket etch rates are: (a) 394 ± 3.9 nm/min, (b) 74.3 ± 0.9 nm/min, (c) 409.2 ± 6.3 nm/min and (d) 119.5 ± 1.7 nm/min. The iso-sidewall taper angles are: (a) 109.7° ± 1.25°, (b) 107.5° ± 0.4°, (c) 110.6° ± 0.55° and (d) 100.7° ± 1.3°.

For a short T_{on} of 2 ms in condition (d), SiCl decays much faster compared to the other cases. Under our experimental conditions, the characteristic diffusion time of SiCl to the wafer surface 2 cm below the measurement region is only a few hundred microseconds. This is much shorter than the gas residence time of about 0.5 s, indicating that radical decay during the afterglow is dominated by diffusion and sticking to the adjacent surfaces rather than evacuation by the vacuum pump [15, 32, 33]. The wall loss rate is determined by the condition of the walls. The similar decay loss rates for cases (a) and (c) suggest that their wall condition is similar. This is consistent with the similar saturated SiCl LIF intensity observed for these two cases (figure 5(a)). The faster off-time decay for case (b) compared to cases (a) and (c) suggests that the wall has a lower deposition for case (b), allowing efficient sticking of SiCl to the wall [34, 35]. A longer off-time likely allows more desorption from the wall surface.

Figure 5(a) shows the absolute SiCl LIF intensities for these four cases. The large DC cases of (a) and (c) reach the same saturated SiCl LIF intensity, suggesting that the saturated $SiCl_2$ densities for these two cases are similar. Despite having the same T_{on} of 7 ms, the level of saturated SiCl generated by case (b) is a few times smaller than case (a). This suggests that the density of $SiCl_2$ generated for case (a) is higher than for case (b), as confirmed in figure 5(b). The longer T_{off} for case (b) results in a lower mean $SiCl_2$ density as $SiCl_2$ decays completely during the long off-time, while it likely only decays partially in $T_{off} = 3$ ms for case (a). The level of SiCl reached for case (d) is an order of magnitude lower than the other cases. A short T_{on} of 2 ms does not allow sufficient SiCl to be produced during the on-phase. This is consistent with the observation that case (d) yielded the lowest $SiCl_2$ density among the four conditions (figure 5(b)). It also results in a cleaner wall that allows by-products to stick easily to the wall surface and results in the fastest off-time decay of SiCl among the four cases (figure 4(b)). Despite having different mean SiCl densities, the silicon blanket etch rate per on-time for these four conditions was nearly the same (data not shown). This further indicates that the measured SiCl density is not solely determined by direct removal from the wafer surface. Figure 5(b) shows the $SiCl_2$ LIF intensity for the four conditions described in table 2. Similar to SiCl radicals, the saturated $SiCl_2$ density during the on-phase for the large DC conditions (a) and (c) are similar. However, the saturated $SiCl_2$ density for case (b) with the small DC, but an on-time of 7 ms is also similar to cases (a) and (c). $SiCl_2$ radicals are produced from the wafer and a sufficiently large on-time dictates the saturated density during the on-phase. When the on-time is set to 2 ms, sufficient time is not provided for $SiCl_2$ to reach this saturated values and results in a lower peak $SiCl_2$ density.

Figure 6 compares the TEM images for the four cases in table 2. The etching time was adjusted to achieve similar etch depths for the four cases. While the sidewall etch profile of the dense features for all the cases looks similar, the sidewall etch profiles of the isolated features are drastically different. The isolated sidewall etch features etched in cases (a), (b), and (c) exhibited a more tapered sidewall angle compared to case (d). These three cases produced a saturated SiCl LIF intensity that is similar within a few times from each other (figure 5(a)). In contrast, case (d) produced isolated sidewall etch features with nearly vertical sidewalls. For this case, SiCl did not grow to its saturation level during the power on-phase and the maximum SiCl LIF intensity was an order of magnitude lower compared to the other

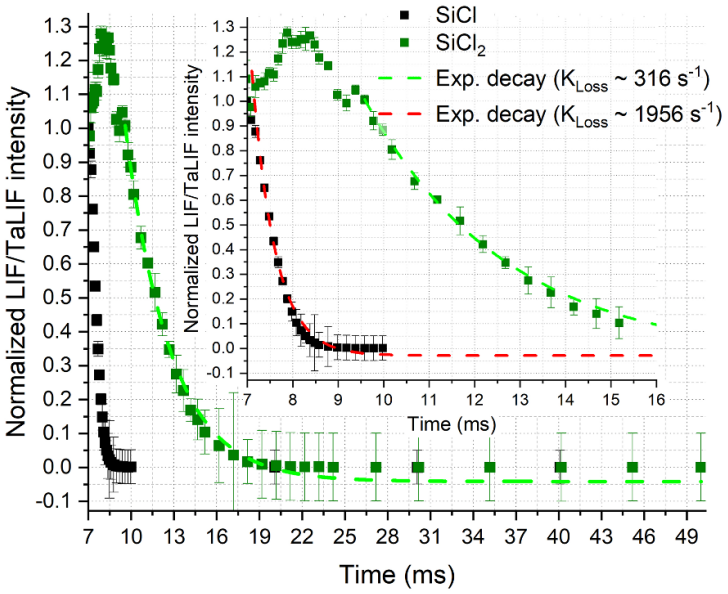


Figure 7. The time-resolved decay of the normalized SiCl and $SiCl_2$ LIF intensities for the power scheme (b) described in table 2.

cases (figure 5(a)). The observed reduction in SiCl density correlates with the formation of nearly vertical isolated sidewalls, supporting the hypothesis that the minimizing of SiCl radicals improves the verticality of the etch profile. A condition may exist in which maintenance of a short on-time and a long off-time completely eliminates the production of SiCl radicals. However, having such an extremely short on-time and long off-time likely results in an unreasonably low etch rate. These measurements provide a baseline for further process optimization to have a vertical isolated sidewall etch profile together with a proficient etch rate.

3.4. Decay of SiCl and $SiCl_2$ radicals

Figure 7 shows the SiCl and $SiCl_2$ decay rates for condition (b) described in table 2. All produced reactive species are lost by evacuation by the vacuum pump, diffusion to the chamber walls or gas-phase reactions. The afterglow loss of these radicals through losses to the wall, gas-phase reactions and vacuum pump evacuation can be estimated by the following equation.

$$\frac{\mathrm{d}[X]}{\mathrm{d}t} = -k_{\mathrm{loss}}[X] = -\left(k_{\mathrm{wall}} + \sum_{R} k_R[R] + k_{\mathrm{pump}}\right)[X] \tag{1}$$

where $[X]$ is the density of SiCl or $SiCl_2$ radicals, k is the reaction rate coefficient and R is the species that the species react in the gas phase. For our experimental conditions, the characteristic evacuation time by the vacuum pump is about 0.5 s. This is much larger than the millisecond range times we observe for SiCl and $SiCl_2$ radicals. The wall loss rate can be estimated by the following equation.

$$\frac{1}{k_{\mathrm{wall}}} = \frac{\Delta^2}{D} + \frac{V}{A}\frac{2(2-\alpha)}{v_{\mathrm{th}}\alpha} \tag{2}$$

where Λ is the characteristic diffusion length, D is the diffusion coefficient, v_{th} is the mean thermal speed of the radicals, V/A the volume-to-surface ratio of the reactor and α is the sticking coefficient of the radicals to the chamber walls. Despite assuming a maximum sticking coefficient value of α equaling one, the maximum loss rate for SiCl radicals considering the wall losses and vacuum pump evacuation is only 500 s^{-1}. However, the decay of SiCl radicals as shown in figure 7 results in a loss rate of approximately 1956 s^{-1}. This suggests that a significant pathway for the loss of SiCl radicals is through gas-phase reactions such as $SiCl + Cl_2 \rightarrow SiCl_2 + Cl$. This would be consistent with the increase in the $SiCl_2$ density when the SiCl density decays [33]. $SiCl_2$ radicals decay slower when the power is turned off (figure 7) and can be explained even with a smaller sticking coefficient [15].

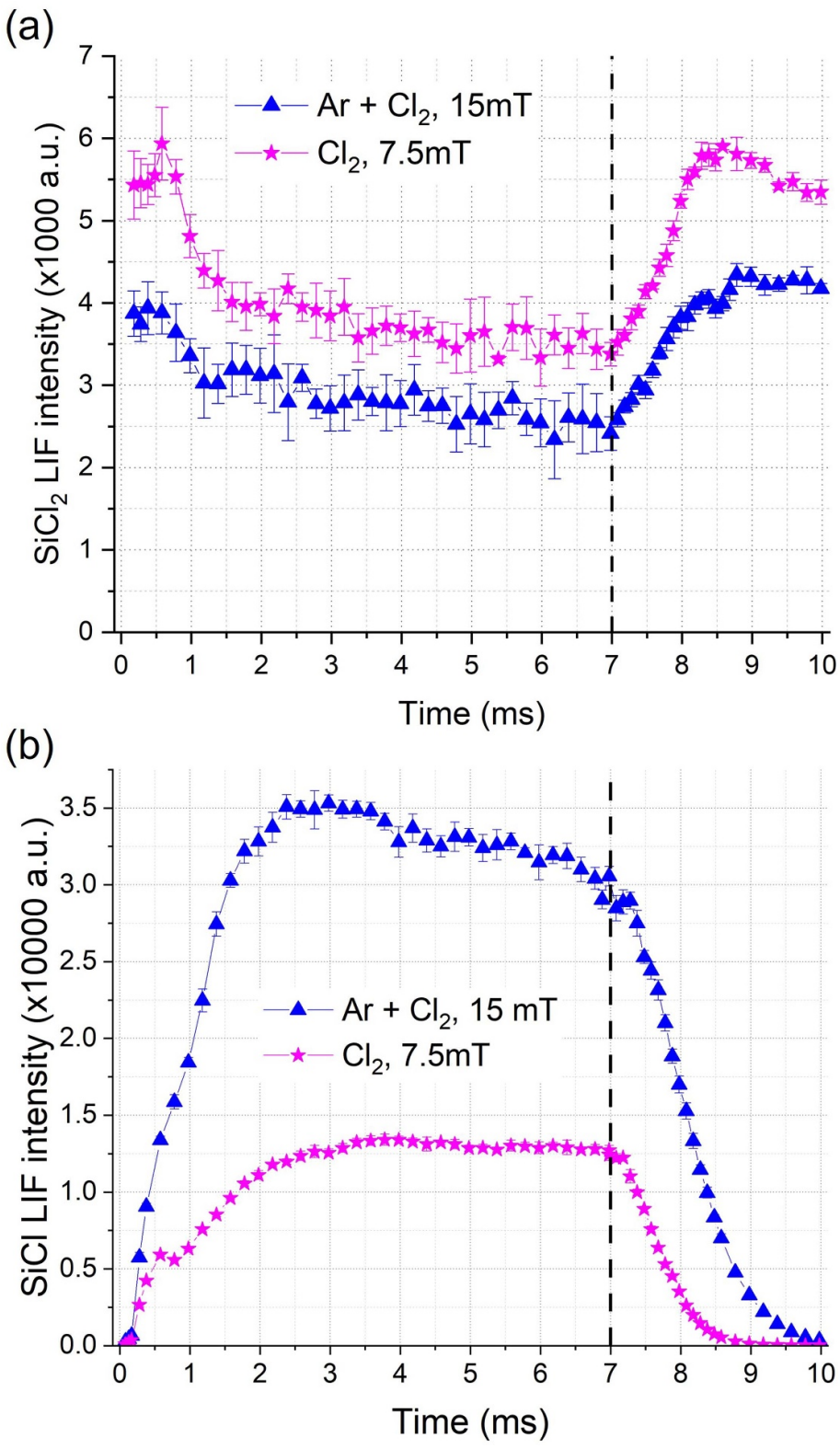


Figure 8. The time-resolved LIF intensities for the power scheme (a) described in table 2 for (a) $SiCl_2$ and (b) SiCl. The gas composition is either 50% Ar + 50% Cl_2 at a pressure of 15 mT or 100% Cl_2 at a pressure of 7.5 mT.

3.5. Effect of argon admixture

Figures 8(a) and (b) compares the time evolution of SiCl and $SiCl_2$ LIF intensities for condition (a) in table 2 using two gas compositions: 50% Ar + 50% Cl_2 at 15 mTorr and 100% Cl_2 at 7.5 mTorr, corresponding to the same partial pressure of Cl_2. This comparison isolates the role of argon in influencing radical production, transport, and loss mechanisms while maintaining similar chlorine availability.

A clear distinction is observed in the behavior of $SiCl_2$ densities between the two gas mixtures. The $SiCl_2$ LIF intensity is consistently higher in the 100% Cl_2 plasma, exceeding that in the Ar-containing plasma by approximately 33% during both the plasma on-phase and the off-phase. This indicates that $SiCl_2$, which is generated both from the wafer surface and the chamber wall deposition, accumulates more efficiently in pure Cl_2 plasmas. This would be consistent with a reduced electron density and absence of argon metastables in pure Cl_2 that likely limits the gas-phase dissociation of $SiCl_2$, allowing a larger steady-state density to be maintained [36, 37]. However, it should be noted that electron densities and argon metastable populations were not directly measured in this study.

In contrast, the presence of argon leads to a substantially enhanced production of SiCl radicals. During the on-phase, the saturated SiCl LIF intensity in the 50% Ar + 50% Cl_2 plasma is nearly three times larger than that measured in the pure Cl_2 plasma. This enhancement is accompanied by a slower decay of SiCl during the afterglow when argon is present. This suggests that the presence of argon strongly promotes the gas-phase conversion of silicon chlorides ($SiCl_x$, $x = 2-4$) into SiCl through increased electron-impact dissociation and potentially through energy transfer from long-lived argon metastables, with $SiCl_2$ being strongly affected. The observed behavior is consistent with an increased electron density in Ar + Cl_2 plasmas compared to a pure Cl_2 plasmas [38]. As a result, $SiCl_2$ is depleted more efficiently in the Ar-containing plasma, while SiCl is both produced in larger quantities during the on-phase and sustained for a longer time during the off-phase. In addition, replacing Ar + Cl_2 with pure Cl_2 likely modifies the electron density and electron energy distribution [38], which can further alter the dissociation kinetics of silicon chloride precursor species. Although electron and argon metastable densities were not measured in the present work, the results indicate that argon affects SiCl production through changes in the underlying plasma kinetics rather than simply through dilution effects.

The opposite trends observed for $SiCl_2$ and SiCl densities highlight the distinct roles of surface-driven production and gas-phase transformation processes in determining radical populations. While $SiCl_2$ density is governed primarily by surface reactions and is higher in pure Cl_2 plasmas, the formation and persistence of SiCl radicals are strongly controlled by gas-phase plasma kinetics that are significantly altered by argon admixture.

4. Conclusion

This work demonstrates that gas-phase SiCl radical dynamics plays a central role in determining the verticality of the sidewall profile during silicon plasma etching in pulsed ICPs with direct current PB. SiCl radicals are produced through a combination of gas-phase dissociation of higher silicon chlorides such as $SiCl_2$, $SiCl_3$ and $SiCl_4$, and surface-generated pathways, with gas-phase dissociation making a major contribution under our experimental conditions. While SiCl production is enhanced in the presence of argon in the gas phase, $SiCl_2$ density is lower in the presence of argon. These results suggest that argon substantially alters the plasma kinetics governing silicon chloride dissociation, potentially through increased electron density and argon metastable assisted processes. Using time-resolved LIF measurements in conjunction with TEM, we show that the modulation of plasma pulse parameters enables direct control of SiCl radical generation and decay. In particular, shorter on-times combined with extended off-times limit radical accumulation by limiting their buildup and persistence of precursor species, resulting in substantially reduced SiCl densities and near-vertical sidewalls in isolated features. In contrast, longer on-times or shorter off-times lead to elevated radical densities and increased sidewall taper, highlighting the strong sensitivity of etch profiles to pulsed plasma conditions. Our findings demonstrate that limiting the plasma on-time directly manipulates the transient production, transport and loss balance of depositing radicals, providing a fundamental route to control high sticking coefficient by-product accumulation and the resulting sidewall profile. The sensitivity of profile verticality to these dynamics underscores the broader importance of understanding the behavior of etch by-products during plasma pulsing for continued scaling in nanoscale fabrication.

Acknowledgments

This work is supported by Applied Materials & a Cooperative Research and Development Agreement (CRADA) between the Princeton Plasma Physics Laboratory and Applied Materials through the U.S. Department of Energy (contract DE-AC02-09CH11466). The authors thank Evgeny Kamenetskiy and

Andrei Khomenko for technical help in setting up and reactor operation. The authors thank Shahid Rauf for discussions of the results.

Data availability statement

The data cannot be made publicly available upon publication because they contain commercially sensitive information. The data that support the findings of this study are available upon reasonable request from the authors.

Author contributions

V S Santosh K Kondeti 0000-0001-8825-845X
Conceptualization (equal), Data curation (equal), Formal analysis (equal), Funding acquisition (equal), Investigation (equal), Methodology (equal), Project administration (equal), Resources (equal), Software (equal), Supervision (equal), Validation (equal), Visualization (equal), Writing – original draft (equal), Writing – review & editing (equal)

Leonid Dorf
Conceptualization (equal), Data curation (equal), Formal analysis (equal), Funding acquisition (equal), Investigation (equal), Methodology (equal), Project administration (equal), Resources (equal), Software (equal), Supervision (equal), Validation (equal), Visualization (equal), Writing – original draft (equal), Writing – review & editing (equal)

Zihao Ding 0000-0002-3496-4065
Conceptualization (equal), Data curation (equal), Formal analysis (equal), Funding acquisition (equal), Investigation (equal), Methodology (equal), Project administration (equal), Resources (equal), Software (equal), Supervision (equal), Validation (equal), Visualization (equal), Writing – original draft (equal), Writing – review & editing (equal)

Sonam D Sherpa 0009-0007-0326-545X
Conceptualization (equal), Data curation (equal), Formal analysis (equal), Funding acquisition (equal), Investigation (equal), Methodology (equal), Project administration (equal), Resources (equal), Software (equal), Supervision (equal), Validation (equal), Visualization (equal), Writing – original draft (equal), Writing – review & editing (equal)

Takumi Yanagawa 0009-0002-6012-6935
Conceptualization (equal), Data curation (equal), Formal analysis (equal), Funding acquisition (equal), Investigation (equal), Methodology (equal), Project administration (equal), Resources (equal), Software (equal), Supervision (equal), Validation (equal), Visualization (equal), Writing – original draft (equal), Writing – review & editing (equal)

Leonid Belau
Conceptualization (equal), Data curation (equal), Formal analysis (equal), Funding acquisition (equal), Investigation (equal), Methodology (equal), Project administration (equal), Resources (equal), Software (equal), Supervision (equal), Validation (equal), Visualization (equal), Writing – original draft (equal), Writing – review & editing (equal)

Yevgeny Raitses 0000-0002-9382-9963
Conceptualization (equal), Data curation (equal), Formal analysis (equal), Funding acquisition (equal), Investigation (equal), Methodology (equal), Project administration (equal), Resources (equal), Software (equal), Supervision (equal), Validation (equal), Visualization (equal), Writing – original draft (equal), Writing – review & editing (equal)

References

[1] Wu B, Kumar A and Pamarthy S 2010 *J. Appl. Phys.* **108** 5
[2] Kim D S, Kim J B, Ahn D W, Choe J H, Kim J S, Jung E S and Pyo S G 2023 *Electron. Mater. Lett.* **19** 424–41
[3] Lill T 2021 *Atomic Layer Processing: Semiconductor Dry Etching Technology* (Wiley)
[4] Cunge G, Kogelschatz M, Joubert O and Sadeghi N 2005 *Plasma Sources Sci. Technol.* **14** S42
[5] Donnelly V M and Kornblit A 2013 *J. Vac. Sci. Technol. A* **31** 050825

[6] Wang P, Wang J and Fang F 2021 *Nanomanuf. Metrol.* **4** 216–25
[7] Smith P and Cao P L 1995 *J. Phys.: Condens. Matter* **7** 7125
[8] Halicioglu T and Srivastava D 1999 *Surf. Sci.* **437** L773–8
[9] Kim H J, Wen L, San Kim D, Kim K H, Hong J W, Chang W J, Namgoong S, Kim D W and Yeom G Y 2022 *Appl. Surf. Sci.* **596** 153604
[10] Knizikevičius R 2003 *Surf. Sci.* **531** L347–50
[11] De Wijs G, De Vita A and Selloni A 1998 *Phys. Rev. B* **57** 10021
[12] Shudo K, Kirimura T, Tanaka Y, Ishikawa T and Tanaka M 2006 *Surf. Sci.* **600** 3147–53
[13] Sakurai S and Nakayama T 2002 *Jpn. J. Appl. Phys.* **41** 2171
[14] De Wijs G A, De Vita A and Selloni A 1997 *Phys. Rev. Lett.* **78** 4877
[15] Cunge G, Kogelschatz M and Sadeghi N 2004 *J. Appl. Phys.* **96** 4578–87
[16] Dorf L *et al* 2022 Plasma processing assembly using pulsed-voltage and radio-frequency power *US Patent App.* 17/315,256
[17] Dorf L *et al* 2023 Plasma processing assembly using pulsed-voltage and radio-frequency power *US Patent* 11,776,789
[18] Dorf L *et al* 2023 Plasma processing assembly using pulsed-voltage and radio-frequency power*US Patent App.* 17/959,074
[19] Dorf L, Dhindsa R, Rogers J, Byun D S, Kamenetskiy E, Guo Y, Ramaswamy K, Todorow V N and Luere O 2023 Plasma processing using pulsed-voltage and radio-frequency power *US Patent* 11,848,176
[20] Singleton S, McKendrick K G, Copeland R A and Jeffries J B 1992 *J. Phys. Chem.* **96** 9703–9
[21] Herman I P, Donnelly V M, Cheng C C and Guinn K V 1996 *Jpn. J. Appl. Phys.* **35** 2410
[22] Herman I, Donnelly V, Guinn K and Cheng C 1994 *Phys. Rev. Lett.* **72** 2801
[23] Cheng C, Guinn K, Herman I and Donnelly V 1995 *J. Vac. Sci. Technol. A* **13** 1970–6
[24] Fuller N, Telesca J D A, Donnelly V M and Herman I P 2003 *Appl. Phys. Lett.* **82** 4663–5
[25] Kondeti V S S K, Yatom S, Romadanov I, Raitses Y, Dorf L and Khomenko A 2024 *J. Vac. Sci. Technol. A* **42** 063005
[26] Meijer G, Heinze J, Meerts W L, Ter Meulen J and Hougen J T 1989 *J. Mol. Spectrosc.* **138** 251–63
[27] Suzuki M, Washida N and Inoue G 1986 *Chem. Phys. Lett.* **131** 24–30
[28] Karolczak J and Clouthier D J 1993 *Chem. Phys. Lett.* **201** 409–15
[29] Tezaki A, Morita K and Matsui H 1994 *J. Phys. Chem.* **98** 10529–34
[30] Vella J R, Elgarhy M A I, Hao Q, Donnelly V M and Graves D B 2024 *J. Vac. Sci. Technol. A* **42** 042604
[31] Hao Q, Kim P, Nam S K, Kang S Y and Donnelly V M 2023 *J. Vac. Sci. Technol. A* **41** 032605
[32] Cunge G, Bodart P, Brihoum M, Boulard F, Chevolleau T and Sadeghi N 2012 *Plasma Sources Sci. Technol.* **21** 024006
[33] Cunge G, Vempaire D, Ramos R, Touzeau M, Joubert O, Bodard P and Sadeghi N 2010 *Plasma Sources Sci. Technol.* **19** 034017
[34] Agarwal A and Kushner M J 2008 *J. Vac. Sci. Technol. A* **26** 498–512
[35] Kim T W and Aydil E S 2003 *J. Electrochem. Soc.* **150** G418
[36] Bassett N L and Economou D J 1994 *J. Appl. Phys.* **75** 1931–9
[37] Lee C and Lieberman M 1995 *J. Vac. Sci. Technol. A* **13** 368–80
[38] Corr C, Despiau-Pujo E, Chabert P, Graham W, Marro F and Graves D B 2008 *J. Phys. D: Appl. Phys.* **41** 185202